ORIGINAL ARTICLE

Droperidol as a potential inhibitor of acyl-homoserine lactone synthase from *A. baumannii*: insights from virtual screening, MD simulations and MM/PBSA calculations

Rajat Kumar Jha[1] · Ekampreet Singh[1] · Rameez Jabeer Khan[1] · Ankit Kumar[1] · Monika Jain[1] ·
Jayaraman Muthukumaran[1] · Amit Kumar Singh[1]

Abstract

Acinetobacter baumannii belongs to the ESKAPE family of pathogens and is a multi-drug resistant, gram-negative bacteria which follows the anaerobic form of respiration. *A. baumannii* is known to be the causative agent of hospital-related infections such as pneumonia, meningitis, endocarditis, septicaemia and a plethora of infections such as urinary tract infections found primarily in immunocompromised patients. These attributes of *A. baumannii* make it a priority pathogen against which potential therapeutic agents need to be developed. *A. baumannii* employs the formation of a biofilm to insulate its colonies from the outer environment, which allows it to grow under harsh environmental conditions and develop resistance against various drug molecules. Acyl-homoserine lactone synthase (AHLS) is an enzyme involved in the quorum-sensing pathway in *A. baumannii*, which is responsible for the synthesis of signal molecules known as acyl-homoserine lactones, which trigger the signalling pathway to regulate the factors involved in biofilm formation and regulation. The present study utilised a homology-modelled structure of AHLS to virtually screen it against the ZINC in trial/FDA-approved drug molecule library to find a subset of potential lead candidates. These molecules were then filtered based on Lipinski's, toxicological and ADME properties, binding affinity, and interaction patterns to delineate lead molecules. Finally, three promising molecules were selected, and their estimated binding affinity values were corroborated using AutoDock 4.2. The identified molecules and a control molecule were subsequently subjected to MD simulations to mimic the physiological conditions of protein ligand-binding interaction under the influence of a GROMOS forcefield. The global and essential dynamics analyses and MM/PBSA based binding free energy computations suggested Droperidol and Cipargamin as potential inhibitors against the binding site of AHLS from *A. baumannii*. The binding free energy calculations based on the MM/PBSA method showed excellent results for Droperidol (− 50.02 ± 4.67 kcal/mol) and Cipargamin (− 42.29 ± 4.05 kcal/mol).

✉ Jayaraman Muthukumaran
  j.muthukumaran@sharda.ac.in

✉ Amit Kumar Singh
  amitk.singh@sharda.ac.in

1 Department of Biotechnology, School of Engineering
   and Technology, Sharda University, Greater Noida,
   U.P. P.C. 201310, India

Graphical abstract
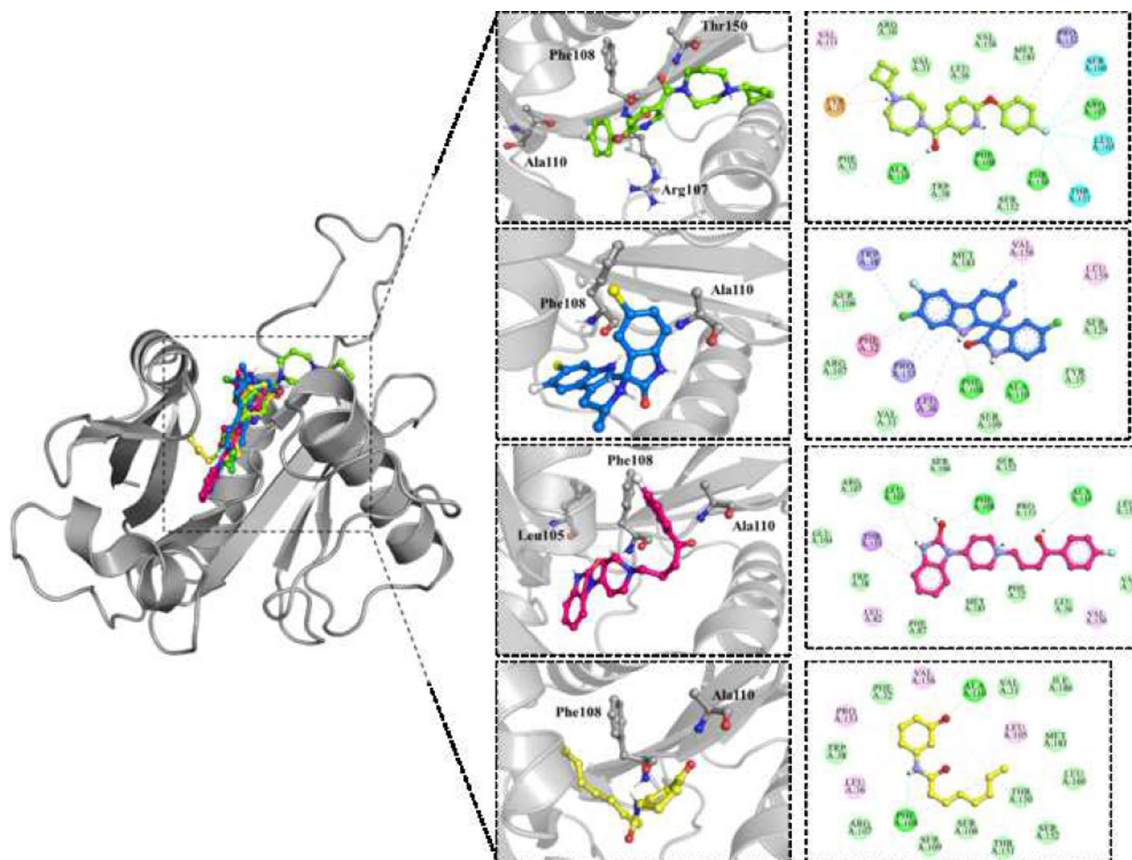
Abbreviations

ADME	Absorption, distribution, metabolism and excretion
DCCM	Dynamical cross-correlation matrix
FEL	Free energy landscape
MD	Molecular dynamics
MM/PBSA	Molecular mechanics/Poisson–Boltzmann surface area

Introduction

Belonging to the ESKAPE (*Enterococcus faecium, Staphylococcus aureus, Klebsiella pneumoniae, Acinetobacter baumannii, Pseudomonas aeruginosa, and Enterobacter*) family of pathogens, *A. baumannii* is a gram-negative bacterium which is found ubiquitously in nature [1, 2]. *A. baumannii* is an anaerobic coccobacillus and is implicated as a causal agent for hospital-related infections, which involves pneumonia, meningitis, endocarditis, septicaemia and a plethora of infections such as urinary tract infections found primarily in immunocompromised patients [3, 4]. *A. baumannii* is known to display multi-drug resistance against diverse classes of antibiotics which can be attributed to the extensive use of antibiotics in clinical practice [1]. Due to the resistance acquired by *A. baumannii,* it is now known to be causative of bloodstream infections in 1–2% of all worldwide infections along with an increased ICU mortality rate of ventilator-assisted pneumonia of approximately 25%. This trend of increased infections on a global scale caused by *A baumannii* has made it a priority pathogen against which new therapeutics need to be discovered [5].

The pathogenesis of *A baumannii* includes the formation of biofilms which is a virulence factor that involves the formation of a protective film which provides the bacteria isolation from the outer environment [6]. This allows the bacteria to grow unhindered under harsh conditions and allows the bacteria to develop resistance to various antibiotics [7, 8]. This attribute of biofilm formation is part of the quorum-sensing pathway found in bacteria which aids

in the regulation of the population in a bacterial colony through a cascade of signal transduction pathways which helps establish a channel of communication amongst bacteria within the colony to develop protective layers against the outer environment [9]. In such pathways, regulators or signal molecules are required to initiate and regulate the formation of proteins and other factors involved formation and regulation of biofilms [7]. One such regulators are acyl-homoserine lactones (AHL) which are autoinducers responsible for triggering the signalling pathway. An AHL molecule comprises a homoserine lactone ring which is bonded to a fatty acyl moiety that shows variety in its size and composition based on the bacteria they are found. The fatty acyl chain of an AHL molecule is a crucial factor in different species due to its diversity as the receptor for AHL molecules show specificity towards them based on the length and structure of the fatty acyl chain. These autoinducers are synthesised by specific enzymes, which are together termed acyl-homoserine-lactone synthases or AHL synthase (AHLS) [8]. In *A. baumannii,* the quorum-sensing pathway includes enzymes involved in the synthesis of the signal molecules (AHLS) and the cognate receptor to which the autoinducers ultimately bind to induce gene expression [10]. A transporter protein is involved in the transportation of the fatty acyl chain substrate to AHLS, upon which a lactone ring donor (*S*-adenosyl-L-methionine) leads to the production of AHL molecules. This AHL molecule will ultimately act as signal molecule for its cognate receptor which will lead to the synthesis of factors involved in biofilm formation and regulation. The AHL molecules and its receptors involve themselves in a positive feedback mechanism which regulates the production of AHL molecules and ultimately regulates the quorum sensing pathway in *A baumannii* [11].

The current study employs extensive computational analyses to investigate the ZINC in trial/FDA-approved drug molecules library for potential lead molecules against AHLS from *A. baumannii,* which will disable the production of AHL molecules that may eventually bring a pause to the pathway and ultimately hinder the formation and regulation of biofilms in *A. baumannii*. The study has targeted AHLS's acylated—acyl carrier protein substrate-binding site, hereinafter referred to as the binding site. Also, we have previously targeted AHLS from *A. baumannii* using the structure-based virtual screening approach [12]. The study identified three potential inhibitory molecules from the Enamine advanced collection small molecule library. The present study builds on our previous study by utilising ZINC in trial/FDA-approved drug molecule library to determine higher affinity under investigation/FDA-approved drug molecules against AHLS from *A. baumannii.* The modelled structure of AHLS from our previous study was utilised against which virtual screening, Lipinski's and toxicological screening and molecular docking studies delineated lead molecules which were

then subjected to 100 ns molecular dynamics (MD) simulations. The MD trajectories were analysed using various global and essential dynamics parameters. Finally, Molecular mechanics/Poisson–Boltzmann surface area (MM/PBSA) based binding free energy calculations were implemented to evaluate the stability of the AHLS-ligand complexes. As a result, we have identified two promising lead candidates (Droperidol and Cipargamin) against AHLS from *A. baumannii*.

Methodology

AHLS structure prediction

Our previous study [12] predicted the 3D structure of AHLS from *A. baumannii* using the homology modelling method. The experimentally solved crystal structure of TofI (PDB ID: 3P2H) from *Burkholderia glumae* was used as the template for SwissModel [13] based homology modelling, and the predicted model was further corrected using YASARA [14]. Moreover, the final optimised model of AHLS was submitted to the ModelArchive database and can be accessed at modelarchive.org/doi/10.5452/ma-15kzu. The same AHLS model has been used in the current study. The reader is referred to our previous publication for detailed methodology and results of homology modelling, model optimisation and model evaluation. The results of initial and corrected AHLS model assessments have been presented in the supplementary data.

Virtual screening, Lipinski's rule of five, toxicity and ADME filtering

The AHLS model was virtually screened with a small molecule library comprising approximately 9300 in trial and FDA-approved drug molecules. The virtual screening was accomplished using AutoDock Vina [15] installed on the Drugdiscovery@TACC (Texas Advanced Computing Centre) portal available at *drugdiscovery.tacc.utexas.edu*. The virtual screening search space was constrained to the binding site (acylated—acyl carrier protein substrate-binding site) of AHLS. The binding site amino acid residues were derived from structural superimposition with the selected template structure. TACC portal reverted a list of thousand ligands exhibiting the strongest binding affinity towards AHLS. Next, the thousand ligands were subjected to Data-Warrior [16] for screening based on Lipinski's rule of five parameters and toxicological properties. The ligands that passed Lipinski's rule of five and toxicological filters were then exposed to SwissADME [17] for screening based on pharmacokinetic properties. The AHLS complexes of the top three ligands that passed ADME filters and had the

highest binding affinity towards AHLS were selected for additional evaluations. Moreover, the inhibitor molecule, J8-C8 (PubChem CID: 53239922), present in the crystallographic structure of the template, was used as a control in the virtual screening. J8-C8 has an experimentally determined dissociation constant (K_D) of 3.6 uM with respect to AHLS from *Burkholderia glumae*. AHLS was also screened with J8-C8 using Vina [18].

Molecular docking

AutoDock 4.2.6 [19] and AutoDockTools 1.5.7 were employed to dock the selected ligands to the binding site of AHLS. AutoDock-based docking was performed to corroborate the binding affinity values obtained from virtual screening. The AutoDock search space was confined to the binding site earlier targeted by virtual screening. The following grid dimensions were used for the docking runs: grid_points_X = 60, grid_points_Y = 40, grid_points_Z = 30, grid_center_X = -0.8, grid_center_Y = 79.39 and grid_center_Z = 51.4. Moreover, GA runs and the population size were configured to 1000 and 200, respectively. The maximum number of generations and evaluations were 27,000 and 25,00,000, respectively. The crossover rate and the mutation rate were 0.8 and 0.02, respectively. The output clusters were analysed in AutoDockTools, and the best complexes were selected for the further assessment using MD simulations. The docking results were analysed, and the interaction figures were prepared using PyMOL and BIOVIA Discovery Studio [20].

Molecular dynamics simulations

Native AHLS and its selected ligand-bound complexes were exposed to 100 ns MD simulations using GROMACS 2021.3 [21]. MD simulations were executed to account for protein flexibility and physiological conditions like aqueous environment, temperature, pressure, etc. The protein structure was parametrised using the GROMOS 54A7 force field [22]. The topology files of selected ligands were generated using PRODRG [23]. Native AHLS and its ligand-bound complexes were confined in cubic boxes, and a 1 nm distance was retained between the protein atoms and the edge of the box. The SPC/E water model was utilised to solvate the AHLS systems. LINCS algorithm was used to constrain the bonds involving hydrogen atoms. The steepest descent algorithm was used to minimise the AHLS systems. The maximum energy tolerance and the number of steps were configured to 100 kJ mol^{-1} nm^{-1} and 50,000, respectively. Upon minimisation, the systems were equilibrated in two stages. In the first stage, 1 ns of NVT equilibration was applied, where the number of particles, volume and temperature (300 K) were kept steady. In the next step, 1 ns of NPT equilibration

was applied, where the number of particles, pressure (1 bar) and temperature were kept steady. The Parrinello-Rahman barostat and v-rescale thermostat maintained the required pressure and temperature values. Next, production MD simulations of 100 ns were performed for the AHLS systems. The MD trajectories were analysed using tools built in the GROMACS package and the R-based Bio3D package [24]. The analyses of the AHLS systems were based on global and essential structural parameters, including RMSD (Root Mean Square Deviation), RMSF (Root Mean Square Fluctuation), Rg (Radius of Gyration), SASA (Solvent Accessible Surface Area), H-bonds (intermolecular hydrogen bonds), PCA (Principal Component Analysis), FEL (Free Energy Landscape) and DCCM (Dynamical Cross-Correlation Matrix). The plots for different MD analyses were prepared via Gnuplot.

Binding free energy calculations

The end state MM/PBSA [25] based method was implemented to compute the binding free energy values of AHLS-ligand complexes. The binding free energy values present a general idea regarding the stability of protein–ligand complexes and intermolecular interactions between the protein and ligand molecules. The calculations were performed using *g_mmpbsa* [26]. The binding free energy calculations were performed according to the following equation:

$$\Delta G_{\text{binding}} = \Delta E_{vdw} + \Delta E_{\text{ele}} + \Delta G_{\text{pol}} + \Delta G_{\text{np}}$$

In this equation, ΔE_{vdw}, ΔE_{ele}, ΔG_{pol} and ΔG_{np} signify contributions of Van der Waals energy, electrostatic energy, polar solvation energy and non-polar solvation energy, respectively. $\Delta G_{\text{binding}}$ depicts the binding free energy values of AHLS complex formation. The *g_mmpbsa* tool implements Lennard–Jones and Coulomb potentials to solve Van der Waals and electrostatic contributions. Furthermore, it implements the Poisson–Boltzmann equation to compute polar solvation energy contribution. Finally, SASA only non-polar model was utilised to solve the non-polar energy contribution. For the calculations, the last 20 ns (80–100 ns) of converged AHLS trajectories were considered, and snapshots were captured every 50 ps.

Results

Virtual screening, Lipinski's rule of five, toxicity and ADME filtering

The AHLS model was downloaded from the ModelArchive database and submitted to Drugdiscovery@TACC portal for Vina based virtual screening. The selected library comprised

approximately 9300 in trial or already FDA-approved drug molecules. The binding site residues of AHLS were extracted via structural superimposition with the template structure (PDB ID: 3P2H). The binding site residues conserved across the AHLS model and the template structure included Phe32, Leu36, Trp38, Glu104, Leu105, Arg107, Leu148, Cys184 and Ile186. The conserved residues implied that the binding site is majorly composed of hydrophobic amino acids. The output from the TACC portal contained a list of the top thousand ligand molecules demonstrating the maximum affinity to the binding site of AHLS. Next, the thousand ligands were screened based on Lipinski's and toxicological parameters. The ligand molecules having molecular weight smaller than 500 Da, hydrogen bond acceptors less than 10, hydrogen bond donors less than 5, topological polar surface area values less than 100 $\mathring{A}^2$, rotatable bonds less than 10, positive druglikeness values and consensus octanol–water partition coefficient values less than 5 were selected for further screening. Moreover, ligands having mutagenic, tumorigenic, reproductive effective and irritative effects were also discarded. Out of the

thousand ligands, only 126 ligand molecules passed these filters. The molecules that passed these filters were then subjected to SwissADME for screening based on ADME properties. In SwissADME, the molecules having ESOL (Estimated SOLubility) class—soluble, high gastrointestinal absorption, blood–brain barrier permeable, non-inhibitor of cytochromes P450 or CYP (CYP1A2, CYP2C19, CYP2C9, CYP2D6, and CYP3A4) enzymes, and zero PAINS (Pan-Assay INterference compoundS) alerts were selected for further evaluations. Out of the 126 ligands, only seven ligand molecules passed all these SwissADME filters. Out of the 7 ligands, the top three were chosen for the next stage of evaluations via MD simulations. The three selected ligands were ZINC000053298428, ZINC000049037032 and ZINC000019796080. ZINC000053298428, ZINC000049037032 and ZINC000019796080 exhibited Vina binding affinity values of − 8.5 kcal/mol, − 9.0 kcal/mol and − 8.9 kcal/mol, respectively. Also, the control molecule, J8-C8, exhibited a binding affinity of − 6.0 kcal/mol in virtual screening. Tables 1, 2 and 3 depict Lipinski's rule

Table 1 Lipinski's properties and druglikeness scores of the selected ligands

S/No	Ligand	MW (≤ 500 Da)	rBonds (≤ 10)	HBA (≤ 10)	HBD (≤ 5)	cLogP (≤ 5)	DL
1	ZINC000053298428	384.558	5	5	3	2.3738	2.3921
2	ZINC000049037032	407.379	0	4	4	2.1486	1.3634
3	ZINC000019796080	398.585	6	5	4	3.6261	1.9388
4	J8-C8	239.358	7	3	1	3.2283	− 18.881

MW molecular weight, *rBonds* rotatable bonds, *HBA* hydrogen bond acceptor, *HBD* hydrogen bond donor, *cLogP* consensus octanol–water partition coefficient, *DL* druglikeness

Table 2 Toxicological properties of the selected ligands

S/No	Ligand	Carcinogenic	Mutagenic	Reproducibility	Irritant
1	ZINC000053298428	No	No	No	No
2	ZINC000049037032	No	No	No	No
3	ZINC000019796080	No	No	No	No
4	J8-C8	No	No	No	No

Table 3 ADME profiles of the selected ligands

S/No	Molecule	GI	BBB permeability	TPSA (100 $\mathring{A}^2$)	ESOL class	CYP inhibitor	PAINS alert
1	ZINC000053298428	High	Yes	56.76	Soluble	No	0
2	ZINC000049037032	High	Yes	70.31	Soluble	No	0
3	ZINC000019796080	High	Yes	67.76	Soluble	No	0
4	J8-C8	High	Yes	46.17	Soluble	No	0

GI gastrointestinal absorption, *BBB* blood–brain barrier, *TPSA* total polar surface area, *ESOL* estimated solubility, *CYP* Cytochrome P450 enzymes, *PAINS* Pan-assay interference compounds

of five, toxicological and ADME properties of the selected ligands.

AutoDock calculations

Next, the selected ligands and J8-C8 were docked to the binding site of AHLS using AutoDock 4.2.6. Figure 1 depicts the 2D and 3D interaction patterns in AHLS complexes. Table 4 summarises the interactions between AHLS and the selected ligands.

The AutoDock estimated binding affinity (ΔG) and inhibition constant (Ki) for ZINC000053298428 against AHLS were -9.15 kcal/mol and 196.21 nM, respectively. The ligand was involved in intermolecular hydrogen bonds with Arg107 (2.8 Å), Phe108 (2.13 Å), Ala110 (2.12 Å) and Thr150 (2.95 Å). The ligand was involved in pi-alkyl interactions with Tyr35 (5.13 Å) and Pro153 (4.81 Å).

Tyr35 (2.61 Å) was also engaged in pi-cation interaction with the ligand molecule. Val111 (5.04 Å) was involved in alkyl-hydrophobic interaction with the ligand. Also, the ligand made halogen (fluorine) bonds with Leu105 (2.95 Å) and Thr151 (3.68 Å). Finally, Arg30, Val31, Phe32, Leu36, Trp38, Ser152, Val156 and Met181 participated in Van der Waals interactions with the ligand molecule.

The AutoDock estimated binding affinity (ΔG) and inhibition constant (Ki) for ZINC000049037032 were − 7.14 kcal/mol and 5.85 uM, respectively. The ligand made hydrogen bonds with Phe108 (2.16 Å) and Ala110 (2.39 Å). The ligand was engaged in pi-alkyl interactions with Phe32 (5.3 Å), Trp38 (5.22 Å), Ala110 (4.47 Å), Pro153 (4.28 Å and 4.38 Å) and Val156 (5.04 Å and 5.47 Å). Val156 (3.4 Å) and Leu159 (4.04 Å) were involved in alkyl-hydrophobic interactions with the ligand
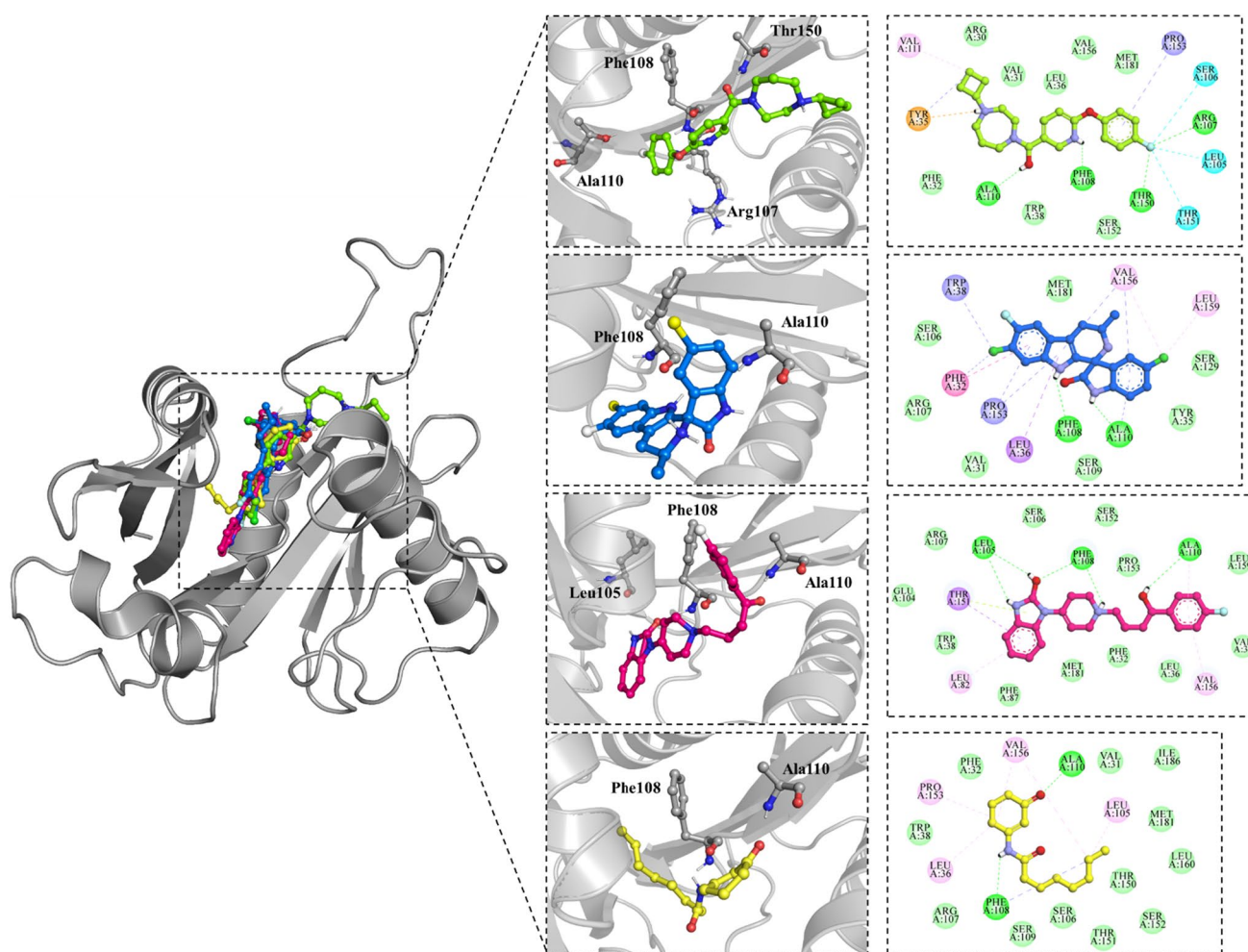

Fig. 1 Selected ligands bound to AHL synthase. Zoomed-in view— Two-dimensional and Three-dimensional illustration of AHLS binding site interacting with ZINC000053298428 (Green: A1 and A2), ZINC000049037032 (Blue: B1 and B2), ZINC000019796080 (Pink: C1 and C2), and J8-C8 (Yellow: D1 and D2) via hydrogen bonds (dark green colour), halogen bonds (sky blue colour), pi-interactions (light pink, orange and purple colour) and Van der Waals interactions (slightly green colour)

Table 4 Intermolecular interactions between selected ligands and AHLS

S/No	Ligands ID	HB	D (Å)	Pi-SR	D (Å)	vdWISR
1	ZINC000053298428	Arg107	2.8	Tyr35	5.13	Arg30, Val31, Phe32, Leu36, Trp38, Ser152, Val156, Met181
		Phe108	2.13	Tyr35	2.61	
		Ala110	2.12	Val111	5.04	
		Thr150	2.95	Pro153	4.81	
2	ZINC000049037032	Phe108	2.16	Phe32	5.24	Val31, Tyr35, Ser106, Arg107, Ser109, Ser129, Met181
		Ala110	2.39	Phe32	5.3	
				Leu36	3.97	
				Trp38	5.22	
				Ala110	4.47	
				Pro153	4.28	
				Pro153	4.38	
				Val156	3.4	
				Val156	5.04	
				Val156	5.47	
				Leu159	4.04	
3	ZINC000019796080	Leu105	3.07	Leu82	5.28	Val31, Phe32, Leu36, Trp38, Phe87, Glu104, Ser106, Arg107, Ser152, Pro153, Leu159, Met181
		Leu105	1.76	Ala110	4.75	
		Phe108	2.11	Thr151	2.61	
		Phe108	1.88	Thr151	2.78	
		Ala110	2.17	Val156	4.35	
4	J8-C8	Phe108	2.19	Leu36	4.99	Val31, Phe32, Trp38, Ser106, Arg107, Ser109, Thr150, Thr15, Ser152, Leu160, Met181, Ile186
		Ala110	1.95	Leu105	4.14	
				Phe108	4.42	
				Pro153	4.58	
				Val156	5.33	
				Val156	5.21	

HB hydrogen bond interaction, *D* distance, *Pi-SR* Pi-interaction sharing residues, *vdWISR* Van der Waals interaction sharing residues

molecule. Leu36 (3.97 Å) made a pi-sigma contact with the ligand molecule. Phe32 (5.24 Å) was also involved in pi-pi T shaped interaction with the ligand molecule. Finally, the ligand participated in Van der Waals contacts with Val31, Tyr35, Ser106, Arg107, Ser109, Ser129 and Met181.

The AutoDock estimated binding affinity (ΔG) and inhibition constant (Ki) for ZINC000019796080 were − 10.23 kcal/mol and 31.69 nM, respectively. The ligand made hydrogen bonds with Leu105 (1.76 Å and 3.07 Å), Phe108 (1.88 Å and 2.11 Å) and Ala110 (2.17 Å). The ligand was engaged in pi-alkyl interactions with Leu82 (5.28 Å), Ala110 (4.75 Å) and Val156 (4.35 Å). Thr151 (2.78 Å) was involved in a pi-lone pair contact with the ligand molecule. Thr151 (2.61 Å) was also involved in pi-sigma interaction with the ligand molecule.

Finally, the ligand was engaged in Van der Waals interactions with Val31, Phe32, Leu36, Trp38, Phe87, Glu104, Ser106, Arg107, Ser152, Pro153, Leu159 and Met181.

The AutoDock estimated binding affinity (ΔG) and inhibition constant (Ki) for J8-C8 were − 6.9 kcal/mol and 8.72 uM, respectively. The ligand was involved in intermolecular hydrogen bonds with Phe108 (2.19 Å) and Ala110 (1.95 Å). The ligand was also engaged in alkyl-hydrophobic interactions with Leu36 (4.99 Å), Leu105 (4.14 Å), Pro153

(4.58 Å) and Val156 (5.33 Å and 5.21 Å). In addition, Phe108 (4.42 Å) was involved in the pi-alkyl interaction. Finally, the ligand was involved in Van der Waals interactions with Val31, Phe32, Trp38, Ser106, Arg107, Ser109, Thr150, Thr15, Ser152, Leu160, Met181 and Ile186. Table 5 compares Vina and AutoDock binding affinities of the selected ligands and also represents their predicted inhibition constants and molecular formulae. Figure 2. Depicts the 2D chemical structures of the selected ligands.

Next, APBS or Adaptive Poisson-Boltzmann Solver PyMOL plugin was executed to compute the electrostatic surface potential of AHLS complexes. The results (see Fig. 3) showed that most of the surface of AHLS comprises slightly acidic or neutral amino acids. In contrast, the binding site of AHLS contains highly basic amino acid residues. Also, the results suggested that the selected ligands adequately occupied the binding site of AHLS.

Molecular dynamics simulations

MD simulations were performed next to reflect the dynamic behaviour of native AHLS and its ligand-bound complexes. AutoDock or Vina doesn't take into account the complete dynamic behaviour of protein molecules, and neither these programmes allow the users to implement essential

Table 5 Chemical formulae, Vina and AutoDock binding affinity and AutoDock inhibition constant of the selected ligands

S/No	Selected ligands	Chemical formula	Vina binding affinity (kcal/mol)	AutoDock binding affinity (kcal/mol)	AutoDock inhibition constant
1	ZINC000053298428 (JNJ-39220675)	$C_{21}H_{24}FN_3O_2$	− 8.5	− 9.15	196.21 nM
2	ZINC000049037032 (Cipargamin)	$C_{19}H_{14}C_{12}FN_3O$	− 9.0	− 7.14	5.85 uM
3	ZINC000019796080 (Droperidol)	$C_{22}H_{22}FN_3O_2$	− 8.9	− 10.23	31.69 nM
4	J8-C8 (Control) (ZINC66157186)	$C_{14}H_{23}NO_2$	− 6.0	− 6.9	8.72 uM

Fig. 2 Ligands selected for molecular docking and molecular dynamics simulation studies
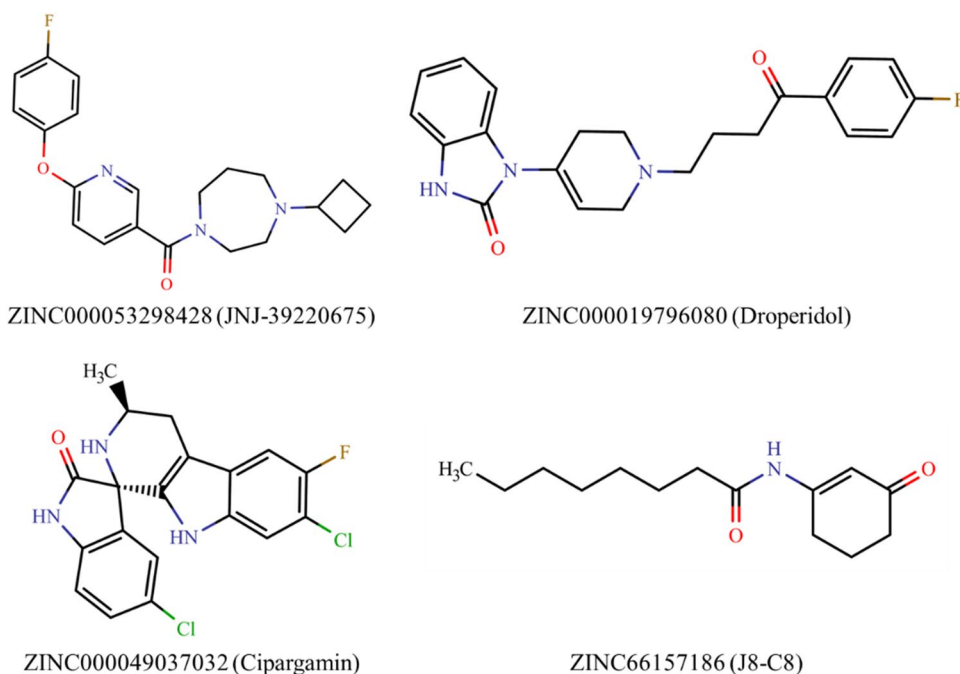
physiological parameters like temperature, pressure, solvation, etc. In contrast, MD simulations provide users with the complete flexibility to study the protein dynamics and implement and perturb the accompanying physiological parameters. The present study has implemented MD simulations to study how the ligand-binding events affected the dynamics of AHLS. The MD trajectories were analysed using global dynamics parameters such as RMSD, RMSF, Rg, SASA, intermolecular hydrogen bonds, and essential dynamics parameters such as PCA, DCCM and FEL. Potential energy (kJ/mol) and temperature (K) plots of AHLS systems after equilibration have been presented in the supplementary data.

In RMSD analysis (see Fig. 4a), the free AHLS system converged at around the 30 ns time point and conserved its stability till the end. In contrast, the AHLS-ligand complexes seemed to attain stability rapidly, but they exhibited increased fluctuations compared to the free protein. For example, the AHLS-ZINC000053298428 complex stabilised

at approximately the 25 ns time point, but it showed noticeable structural fluctuations between the 50–65 ns range. However, the complex stabilised again with a lower average RMSD and maintained it till the end. The AHLS-ZINC000049037032 complex converged at around 20 ns time point and exhibited a very consistent RMSD till the end. The AHLS-ZINC000019796080 complex also converged around the 20 ns time point, but its fluctuations were more pronounced than the AHLS-ZINC000049037032 complex. Finally, the AHLS-J8-C8 complex exhibited the most significant initial fluctuations, stabilised at around the 55 ns time point, and preserved it until the end. The average RMSD values of the native AHLS, AHLS-ZINC000053298428, AHLS-ZINC000049037032, AHLS-ZINC000019796080 and AHLS-J8-C8 complexes were 0.35 nm, 0.43 nm, 0.47 nm, 0.51 nm and 0.46 nm, respectively (rounded off to two decimal places).
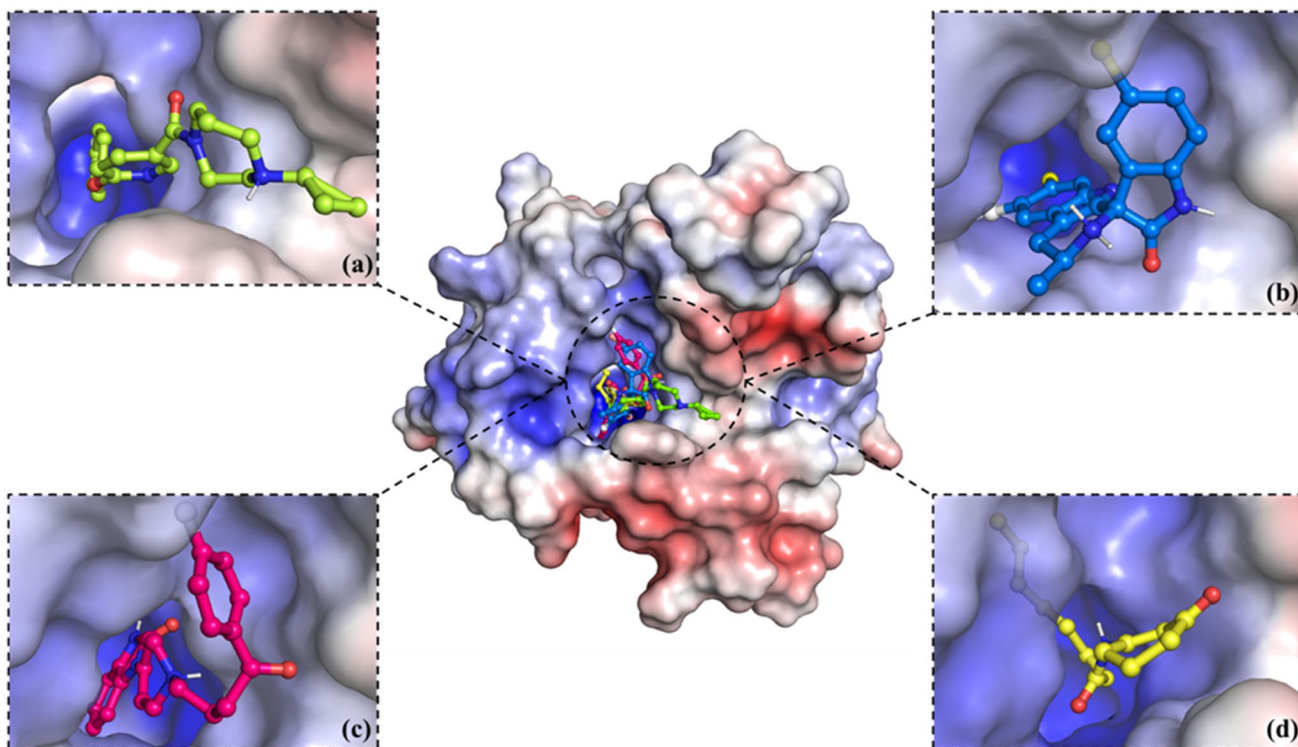
Fig. 3 The electrostatic surface potential of AHLS bound to ZINC000053298428 (Green), ZINC000049037032 (Blue), ZINC000019796080 (Pink), and J8-C8 (Yellow). The red-cultured, blue-coloured and white-coloured patches represent acidic, basic and neutral amino acid residues, respectively
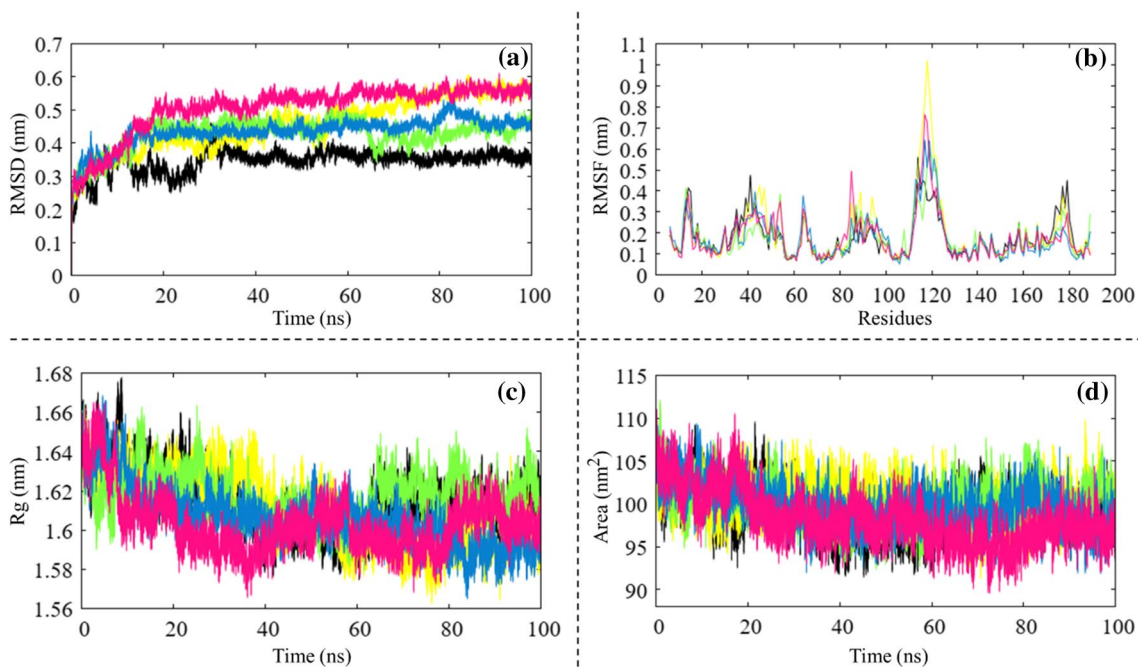

Fig. 4 Analysis of MD simulations of free AHLS (black), AHLS-ZINC000053298428 (green), AHLS-ZINC000049037032 (blue), AHLS-ZINC000019796080 (pink), and AHLS-J8-C8 (yellow) **a** RMSD **b** RMSF **c** Rg **d** SASA

In RMSF analysis (see Fig. 4b), the AHLS systems exhibited enhanced fluctuations in the *N* and *C* terminal ends and the segment comprising 110–125 amino acid residues. The Ala110-Ser125 amino acid residues segment comprises a highly flexible loop, leading to the highest fluctuations in all AHLS systems. Moreover, increased fluctuations were also observed in loop dominated segments comprising residues Tyr35-Gln50 and Leu75-Pro100. The AHLS-J8-C8 complex exhibited the highest RMSF across all AHLS systems. Conversely, the RMSF values exhibited by other AHLS complexes were very comparable. The average RMSF values of the free AHLS, AHLS-ZINC000053298428, AHLS-ZINC000049037032, AHLS-ZINC000019796080 and AHLS-J8-C8 complexes were 0.18 nm, 0.18 nm, 0.18 nm, 0.17 nm and 0.2 nm, respectively (rounded off to two decimal places).

Next, Rg values of AHLS systems were analysed (see Fig. 4c). Except for the native AHLS structure and AHLS-ZINC000053298428 complex, the remaining AHLS systems also showed a slight downward trend in the Rg values. Also, the native AHLS structure exhibited the highest Rg (1.68 nm at 8.69 ns), whereas the AHLS-J8-C8 complex exhibited the lowest Rg (1.56 nm at 76.21 ns) across all systems. Besides, most of the Rg fluctuations were observed in the first 60 ns as the values of all AHLS systems noticeably stabilised after the 60 ns time point. The average Rg values showed by the native AHLS, AHLS-ZINC000053298428, AHLS-ZINC000049037032, AHLS-ZINC000019796080 and AHLS-J8-C8 complexes were 1.62 nm, 1.62 nm, 1.61 nm, 1.6 nm and 1.61 nm, respectively (rounded off to two decimal places).

Next, the perturbations in SASA of AHLS-ligand complexes compared to the native AHLS were analysed (see Fig. 4d). Except for the AHLS-J8-C8 complex, it was observed that the ligand-binding events led to a slight downward trend in the SASA of AHLS. Moreover, the AHLS-ZINC000053298428 complex (111.919 nm^2 at 0.85 ns) registered the highest SASA, whereas the AHLS-ZINC000019796080 complex (89.69 nm^2 at 72.64 ns) registered the lowest SASA out of all AHLS systems. The average SASA values exhibited by the free AHLS, AHLS-ZINC000053298428, AHLS-ZINC000049037032, AHLS-ZINC000019796080 and AHLS-J8-C8 complexes were 99.11 nm^2, 100.1 nm^2, 99.54 nm^2, 98.24 nm^2 and 100.36 nm^2, respectively. Additionally, the protein SASA that got buried ($_{bur}$SASA) or became inaccessible to the solvent because of the ligand-binding events was calculated using the following formula: $_{bur}$SASA = (SASA$_{protein}$ + SASA$_{ligand}$) − SASA$_{complex}$ [27]. Table 6. showcases the individual SASA components and $_{bur}$SASA of AHLS systems. The $_{bur}$SASA of AHLS-ZINC000053298428, AHLS-ZINC000049037032, AHLS-ZINC000019796080 and AHLS-J8-C8 complexes were calculated to be 6.39 nm^2, 7.16 nm^2, 8.51 nm^2 and 6.63 nm^2, respectively (rounded off to two decimal places).

Next, the intermolecular hydrogen bond formation and disruption between AHLS and the selected ligands were analysed (see Fig. 5). The AHLS-ZINC000053298428 involved the least number of hydrogen bonds out of all complexes. On the other hand, the AHLS-ZINC000049037032 complex consistently made two to three H-bonds in the final 40 ns of the MD simulation. Similarly, the AHLS-ZINC000019796080 complex consistently made three H-bonds after the 50 ns time point. The control molecule also made one to two H-bonds throughout the MD simulation. The average H-bonds in AHLS-ZINC000053298428, AHLS-ZINC000049037032, AHLS-ZINC000019796080, and AHLS-J8-C8 complexes were 0, 1, 2 and 1, respectively (rounded off to the nearest whole number).
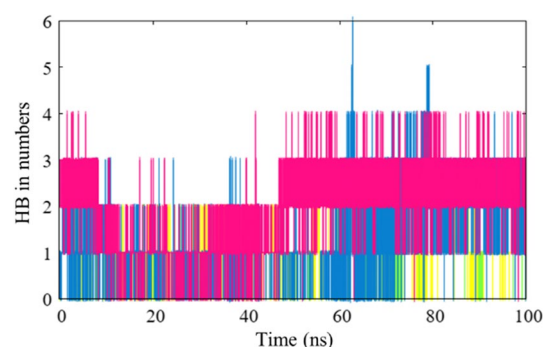

Fig. 5 Hydrogen bond analysis of AHLS-ZINC000053298428 (green), AHLS-ZINC000049037032 (blue), AHLS-ZINC000019796080 (pink), and AHLS-J8-C8 (yellow)

Table 6 Individual SASA components and $_{bur}$SASA of AHLS systems

System	SASA$_{protein}$ (nm^2)	SASA$_{ligand}$ (nm^2)	SASA$_{complex}$ (nm^2)	$_{bur}$SASA (nm^2)
Native AHLS	99.11	–	–	
AHLS-ZINC000053298428	100.19	6.30	100.1	6.39
AHLS-ZINC000049037032	101.22	5.48	99.54	7.16
AHLS-ZINC000019796080	100.61	6.14	98.24	8.51
AHLS-J8-C8	102.31	4.68	100.36	6.63

The biologically relevant, high magnitude and low-frequency motions or essential dynamics of alpha carbons ($C\alpha$) of AHLS systems were extracted using PCA. The eigenvectors were derived from the covariance matrix, and the trajectories were projected on the two-dimensional essential subspace of orthogonal eigenvector 1 (EV1) and eigenvector 2 (EV2). The analysis showed that the top two eigenvectors or principal components (PC1 and PC2) captured 48.7–62.7% of the variance proportion observed in PCA. Figure 6 depicts the 2-D projections of the most significant variances and the eigenvalue ranks of AHLS systems. The blue-coloured dots on the essential subspace represent initial AHLS conformations observed during MD simulation, whereas the white-coloured dots and red-coloured dots represent intermediate and final conformations. Moreover, the gradual transition of blue-coloured dots to white-coloured dots and eventually to red-coloured dots depict the temporal conformational perturbations exhibited by the AHLS systems. The projections suggested that the ligand-binding events lead to distinct perturbations in AHLS essential dynamics compared to the

native AHLS structure. The essential subspace of native AHLS had initial conformations spread out on the right-hand region, which gradually shifted to conformations in the intermediate states in the centre, followed by the tight clustering of final conformations on the left-hand region. For the AHLS-ZINC000053298428 complex, the initial conformations resided on the top right-hand part of the essential subspace, which gradually shifted to intermediate states on the centre-left hand, followed by relatively dispersed clustering of final conformations on the lower right-hand region. For the AHLS-ZINC000049037032 complex, the initial conformations populated the left-hand region of the essential subspace, which shifted to the intermediate state conformations on the lower left-hand part, followed by the compact clustering of final conformations on the lower right-hand region. For the AHLS-ZINC000019796080 complex, the initial conformations were scattered on the essential subspace, which gradually shifted to intermediate states on the upper left-hand part, followed by very compact clustering of final conformations on the lower left-hand region. For
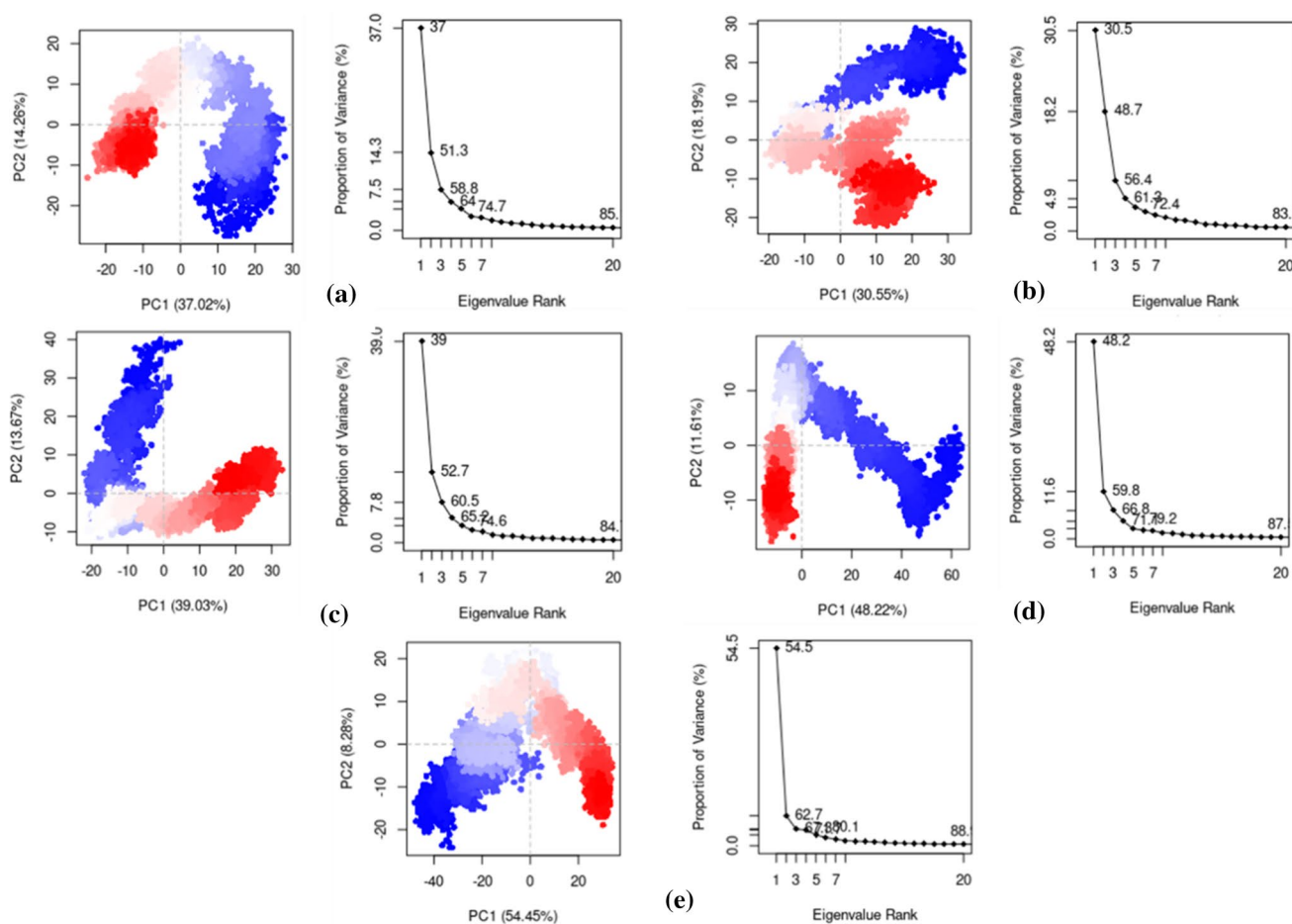

Fig. 6 PCA and eigenvalue ranks of **a** native AHLS, **b** AHLS-ZINC000053298428, **c** AHLS-ZINC000049037032, **d** AHLS-ZINC000019796080, and **e** AHLS-J8-C8

the AHLS-J8-C8 complex, the initial conformations were scattered on the left-hand region of the essential subspace, which transitioned to the intermediate states in the centre, followed by the compact clustering of final conformations on the right-hand region. Furthermore, the top two eigenvectors of native AHLS, AHLS-ZINC000053298428, AHLS-ZINC000049037032, AHLS-ZINC000019796080 and AHLS-J8-C8 complexes captured 51.3%, 48.7%, 52.7%, 59.8% and 62.7% of total variances, respectively.

Next, the modevectors.py script (https://raw.githubuser content.com/Pymol-Scripts/Pymol-script-repo/master/modevectors.py) was used to analyse the contributions of the essential dynamics made by the top two eigenvectors (EV1 and EV2). For each AHLS system, the structures with two extreme states representing the essential dynamics contribution made by EV1 and EV2 were extracted using the *gmx anaeig* module. Next, using the modevectors.py script, spikes were drawn from the alpha carbon ($C\alpha$) atoms of the initial state to the final state of the AHLS structure. The minimum cut-off for the spikes was set to 4 Å in the script, which meant that fluctuations < 4 Å were exempted from this analysis. Also, the length of the spikes was proportional to the $C\alpha$ atomic fluctuations. In Fig. 7, the AHLS structures with red-coloured spikes represent the fluctuations contributed by eigenvector 1 (EV1), whereas the structures

having yellow coloured spikes represent the fluctuations contributed by eigenvector 2 (EV2). The results showed that most of the EV1 and EV2 fluctuations were localised in the highly flexible loop regions (F12-E18 residues, Glu39-Gln50, Glu85-Pro95 residues, Ala110-Val128 residues and Ala170-Leu185 residues) of the native and ligand-bound AHLS structures. Moreover, enhanced fluctuations in loops comprising residues Asp63-Asn67 and Leu91-Ser99 of the AHLS-ZINC000049037032 complex were present. Similarly, in the AHLS-ZINC000019796080 complex, the Glu39-Gln50 segment fluctuations were extended to the Val33-Val54 residues loop segment. Finally, the length of the spikes suggested that AHLS-ZINC000019796080 and AHLS-J8-C8 complexes experienced the highest magnitude essential dynamics across all AHLS systems.

Besides, the top two eigenvectors (EV1 and EV2) were used for the FEL study of AHLS systems. Each AHLS system exhibited a distinct clustering pattern of low energy states. In Fig. 8, the red-coloured regions in the FEL basins represent high energy conformations, whereas purple coloured regions represent the very low energy (Gibbs energy content approaching 0 kJ/mol) conformations. The native AHLS primarily formed three separate low energy basins, and the accompanying minima with flattened ends suggested clustering of low to very low energy conformations
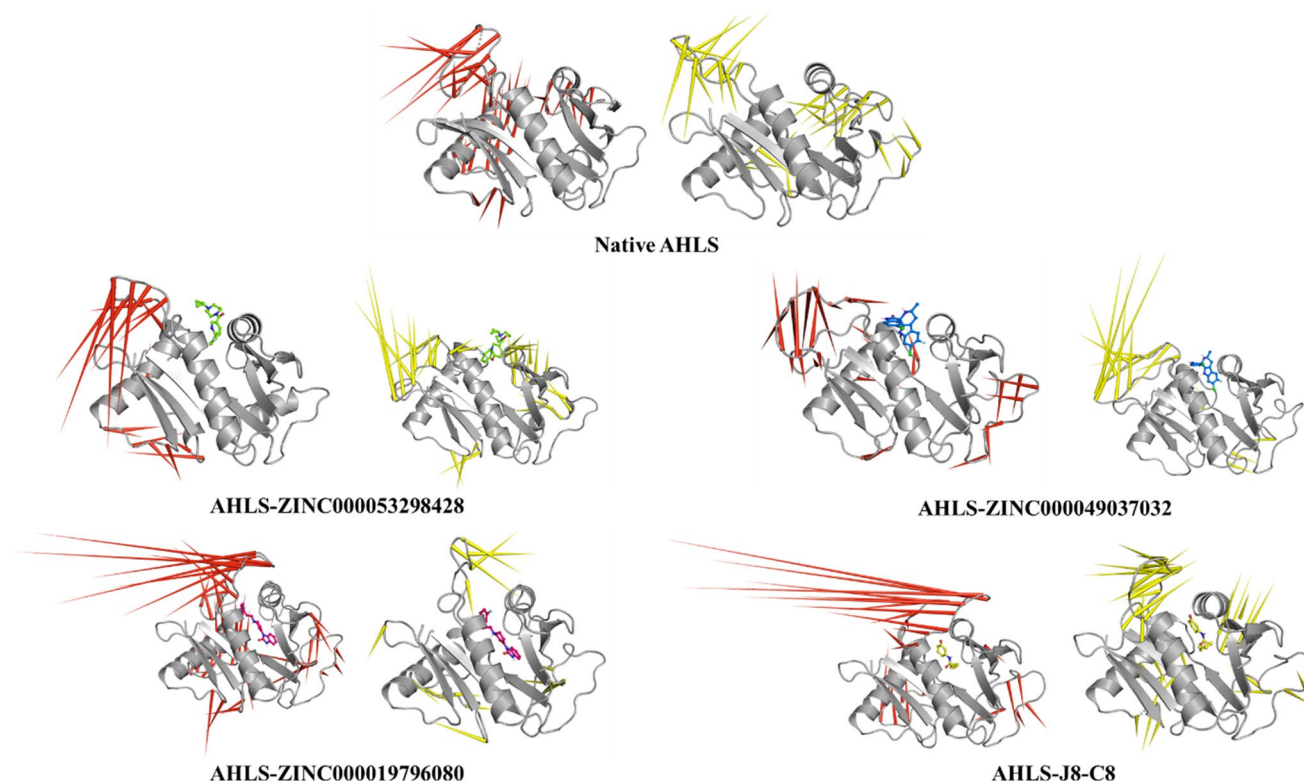

Fig. 7 Essential dynamics analysis of AHLS and its ligand-bound complexes. The red spikes represent the motion contributed by PC1, and the yellow spikes represent the motion contributed by PC2
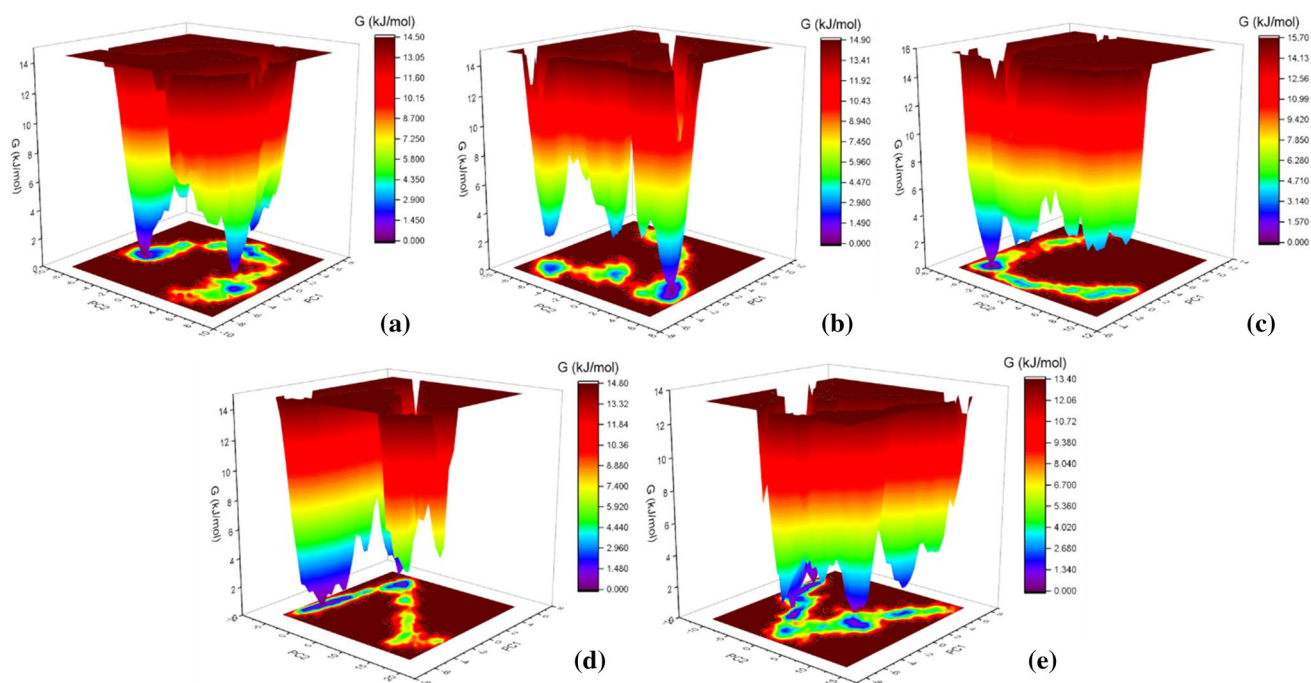
Fig. 8 Free energy landscapes of **a** native AHLS, **b** AHLS-ZINC000053298428, **c** AHLS-ZINC000049037032, **d** AHLS-ZINC000019796080, and **e** AHLS-J8-C8

in all three basins. Upon ZINC000053298428 binding to AHLS, a shift in the coordinates of the low energy basins was observed. Moreover, the basins were noticeably narrower, and the clustered low energy conformations retained relatively higher energy than the low energy conformations of native AHLS. In the case of the AHLS-ZINC000049037032 complex, the low energy basins were further constricted, and conformations residing in only one cluster attained the lowest energy minima. In the case of the AHLS-ZINC000019796080 complex, two very low energy extended basins (connected with a medium energy barrier) populated with conformations in the very low energy state were observed. Finally, the AHLS-J8-C8 complex assumed the most rugged FEL with an extended, very low energy basin occupied by conformations in stable states interconnected with low energy barriers. The presence of minima with flattened ends again suggested the clustering of conformations in low energy stable state at multiple coordinates in the FEL of the AHLS-J8-C8 complex.

Next, the secondary structure components of AHLS systems were analysed using the DSSP programme [28] available for GROMACS. The programme can classify secondary structure elements into the following categories: coil, β-sheet, β-bridge, bend, turn, α-helix and others (π-helix and 3_{10}-helix). Additionally, DSSP recognises α-helix, β-sheet, β-bridge and turn as "structure". The results showed that the percentages of different AHLS secondary structure elements were very consistent during the MD simulations

(see Fig. 9). However, compared to the native AHLS structure, some minor interconversions between the secondary structure elements were observed in AHLS-ligand complexes (see Table 7). For example, the native AHLS structure and AHLS-J8-C8 complex possessed 62% structured elements, whereas AHLS-ZINC000053298428, AHLS-ZINC000049037032, and AHLS-J8-C8 complexes had 59%, 61% and 59% structured elements, respectively. Additionally, the results showed that the ligand-binding events slightly increased ($\Delta = 3\%$) the percentage of bends and slightly decreased ($\Delta = -1\%$) the percentage of π-helices and 3_{10}-helices in the AHLS structure.

The DCCM analysis was executed to study how the ligand-binding events perturbed correlated and anti-correlated motions of amino acid residues of AHLS systems. The motions captured by the top 20 eigenvectors derived from PCA were considered for it. Figure 10 represents the DCCM maps and corresponding molecular visualisation of correlated and anti-correlated motions in AHLS systems. The gradient scale in DCCM maps describes the range of correlated or anti-correlated motions, where 1 (red) means completely correlated motions and -1 (blue) implies completely anti-correlated motions. The circled regions in DCCM plots depict the AHLS segments undergoing the most significant disturbances in correlated or anti-correlated motions. In the 3D visualisations, the red-coloured threads describe pairwise residue cross-correlations, whereas the blue-coloured regions represent anti-correlations. For the native AHLS
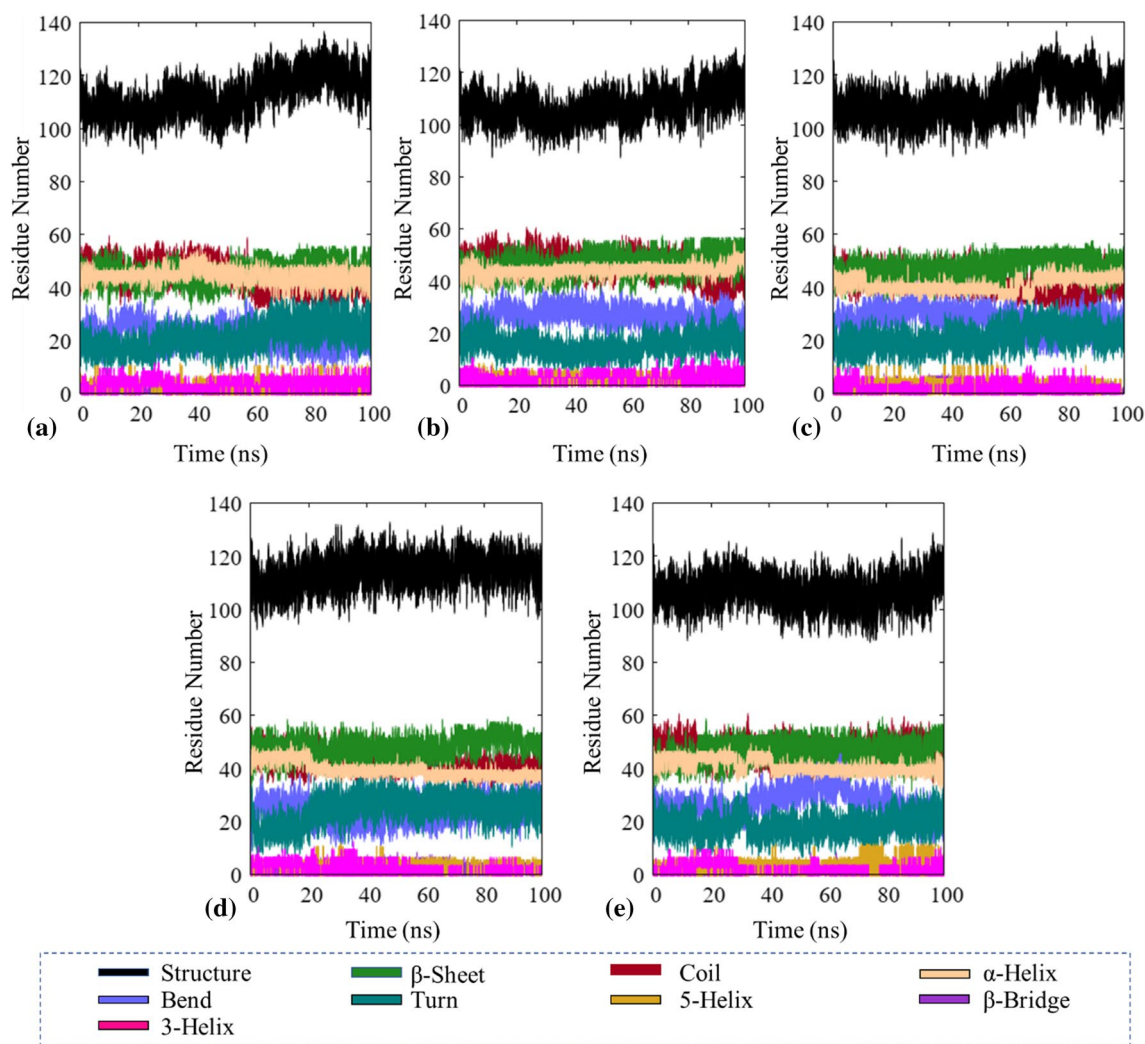
Fig. 9 Secondary structure analysis of **a** native AHLS, **b** AHLS-ZINC000053298428, **c** AHLS-ZINC000049037032, **d** AHLS-ZINC000019796080, and **e** AHLS-J8-C8

Table 7 Secondary structure elements of native AHLS and the selected AHLS-ligand complexes

System	Structure	Coil	β-Sheet	β-Bridge	Bend	Turn	α-Helix	Others
AHLS	62	24	25	0	12	12	24	3
AHLS-ZINC000053298428	59	25	26	0	14	8	24	2
AHLS-ZINC000049037032	61	23	26	1	15	11	22	2
AHLS-ZINC000019796080	62	23	26	1	13	13	22	2
AHLS-J8-C8	59	25	25	1	15	10	22	2

Structure $= \alpha$-Helix $+ \beta$-Sheet $+ \beta$-Bridge $+$ Turn

Others $= \pi$-Helix $+ 3_{10}$-Helix

structure, the results showed that amino acid residues in secondary structure elements exhibited extensive correlated motions. In contrast, anti-correlated motions were observed between the Lys25-Leu40 helix loop segment and the Pro80-Leu90 loop helix segment, Arg30-Leu40 helix loop segment and Pro173-Met181 strand loop strand segment and

Gln143-Gln147 loop segment and Pro173-Met181 strand loop strand segment. The results also showed that the binding of ZINC000053298428 to AHLS resulted in a minor global loss of correlated motions. However, the loss was more pronounced in the case of anti-correlated motions because it caused a significant loss at the substrate-binding

site, and it also resulted in a noticeable gain of anti-correlated motions between the Asn115-Ala123 loop segment and neighbouring secondary structure elements. The binding of ZINC000049037032 to AHLS increased both correlated and anti-correlated motions. Compared to native AHLS, the correlation pattern of the AHLS-ZINC000049037032 appeared to be very similar, but the pattern of non-correlated motions again exhibited significant perturbation and looked like a hybrid of non-correlated motions in native AHLS and AHLS-ZINC000053298428 complex. Most non-correlated motions were observed between the Lys23-Arg30 alpha-helix segment and Asn115-Ala123 loop segment, Ser26-Gly37 alpha-helix segment and Ala170-Pro173 loop segment and Val128-Glu135 alpha helix segment and Asn115-Ala123 loop segment. The binding of ZINC000019796080 also resulted in the gain of both correlated and anti-correlated motions in the AHLS structure. Compared to native AHLS, nearly all secondary structure elements of AHLS-ZINC000019796080 exhibited increased correlated motions. The pattern of anti-correlated motions again looked like a hybrid of non-correlated motions in the native AHLS structure and the AHLS-ZINC000053298428 complex. The majority of non-correlated motions were observed between the Phe87-Leu91 alpha-helix segment and the Phe32-Asn41 segment, Ser114-Ala123 loop segment and Ser129-Asn138 alpha-helix segment, Ser114-Ala123 loop segment and Gln147-Pro153 beta-strand and Ser114-Ala123 loop segment and Phe182-Ile188 beta-strand. Compared to other AHLS ligands, the binding of J8-C8 to AHLS caused the most significant global increase in correlated motions. In the case of anti-correlated motions, the AHLS-J8-C8 complex exhibited a pattern similar to that of the AHLS-ZINC000053298428 complex. Just like the case of ZINC000053298428, the results depicted that the binding of J8-C8 resulted in a significant loss of anti-correlated motions at the substrate-binding site of AHLS, and it also resulted in a substantial gain of anti-correlated motions between Ser114-Ala123 loop segment and Ile149-Arg169 segment, Ser114-Ala123 loop segment and Ser129-Phe139 alpha-helix segment and Ser114-Ala123 loop segment and Ile69-Ala72 beta-strand segment.

Binding free energy calculations

The binding free energy values of AHLS complexes were calculated utilising the end state MM/PBSA method. The per residue binding energy decomposition analysis was also performed to identify the top interacting residues involved in AHLS complex formation. The individual energy components and total binding free energy values of AHLS complexes have been summarised in Table 8 (rounded off to two decimal places). The binding free energy values of AHLS-ZINC000053298428, AHLS-ZINC000049037032,

AHLS-ZINC000019796080 and AHLS-J8-C8 complexes were -57.91 ± 5.57 kcal/mol, -42.29 ± 4.05 kcal/mol, -50.02 ± 4.67 kcal/mol and -17.24 ± 2.38 kcal/mol, respectively ($\pm$ symbolizes standard deviation). The AHLS-ZINC000053298428 complex exhibited noticeable fluctuations in the binding free energy value between 85 to 90 ns and 95 to 100 ns time points; however, the binding free energy value was always lesser than -39.14 kcal/mol. The data depicted that Van der Waals energy and electrostatic energy components made favourable contributions, whereas the contribution of polar solvation energy was unfavourable to AHLS complex formation. The non-polar solvation (SASA) energy component also contributed favourably to AHLS complex formation. Figure 11 depicts the binding free energy values, the contribution of individual amino acid residues and the top 5 (favourable) binding energy contributing residues of AHLS to complex formation. The data showed that acidic amino acid residues (Glu34, Glu39, Asp49, Glu157 and Asp177) were consistently among the top contributors to binding free energy across all the selected AHLS-ligand complexes.

Discussion

The current study incorporates the structure-based drug design approach to identify in trial/FDA-approved drug molecules capable of inhibiting the AHLS from *A. baumannii*. Initially, the binding site of the AHLS model was screened against a library of in trial/FDA approved drug molecules. Next, the high-affinity molecules derived from virtual screening were filtered based on Lipinski's rule of five, toxicological and ADME properties. Finally, three high-affinity molecules with optimal drug-like properties were selected, and then they were re-docked to binding site of AHLS using AutoDock to corroborate the virtual screening binding affinity values. The selected three ligands were ZINC000053298428, ZINC000049037032 and ZINC000019796080, and their AutoDock binding affinity values were -9.15 kcal/mol, -7.14 kcal/mol and -10.23 kcal/mol, respectively. Also, all the estimated inhibition constant values of the selected ligands were < 5.85 uM, and all of them participated in at least two hydrogen-bonding interactions with the residues of the binding site of AHLS. Besides, Vina and AutoDock results suggested that selected ligands exhibited significantly higher binding affinity and improved intermolecular contacts than J8-C8 (control molecule). Furthermore, the binding affinity values obtained from AutoDock and Vina were consistent across all AHLS complexes with maximum binding affinity deviation < 2 kcal/mol.

Next, the stability, compactness and dynamics of unbound AHLS and its complexes in an aqueous solvent

Residue Number

Residue Number

Correlated Motions

Anti-correlated Motions

(a)

(b)

(c)

(d)

(e)

◀**Fig. 10** Dynamical cross-correlation matrix analysis for **a** free AHLS, **b** AHLS-ZINC000053298428, **c** AHLS-ZINC000049037032, **d** AHLS-ZINC000019796080, and **e** AHLS-J8-C8. The circled regions in DCCM plots depict the AHLS segments undergoing the most significant changes in correlated or anti-correlated motions

were evaluated using MD simulations and binding free energy calculations. The RMSD analysis of AHLS systems suggested that complexes formed by ZINC000049037032 and ZINC000019796080 exhibited satisfactorily high stability with average RMSD < 0.51 nm. In comparison, AHLS complexes formed by ZINC000053298428 and J8-C8 exhibited inconsistent RMSD values throughout the MD simulations. The analysis of per residue fluctuation (RMSF) also suggested relatively high stability of all the selected AHLS complexes, with fluctuations only once exceeding the 5 Å mark. Conversely, J8-C8 increased fluctuations in all the loop segments of AHLS. The SASA analysis suggested high structural stability of the selected AHLS-ligand complexes, especially the AHLS- ZINC000019796080 complex, which exhibited the most consistent SASA across all AHLS systems. Next, $_{bur}$SASA measures the interface size between protein–protein or protein–ligand complexes [29], and it has been demonstrated that there is a direct correlation between $_{bur}$SASA and the binding affinity of protein–protein complexes [27]. The results of the $_{bur}$SASA calculation showed that all AHLS complexes experienced noticeable burial in SASA values upon binding to the ligand molecules. The AHLS-ZINC000019796080 complex experienced the maximum burial (8.51 nm^2) and thus had the largest protein–ligand interface across all AHLS complexes, indicating its high structural stability. The Rg analysis indicated that, except for ZINC000053298428, the binding of selected ligands and J8-C8 did not lead to any significant perturbation in overall compactness, and AHLS maintained its optimally folded state during MD simulations. In contrast, the native AHLS structure and AHLS-ZINC000053298428 complex experienced abrupt changes in overall compactness at 60 ns time point and remained stable afterwards. The secondary structure analysis showed that the ligand-binding events did not much influence the composition of secondary structure elements of AHLS. The native AHLS structure and AHLS- ZINC000019796080 complex exhibited 62% structured elements, whereas the other AHLS systems experienced 1% to 3% loss of structured elements. Interestingly, the intermolecular H-bonding analysis depicted that none of the selected ligands or the control molecule was able to maintain the number of hydrogen bonds originally observed during docking calculations. For example, the average number of H-bond for the AHLS-ZINC000053298428 complex dropped to 0, whereas the rest of the AHLS complexes exhibited 1 to 2 time-averaged H-bonds. Upon inspection of the MD simulation trajectory
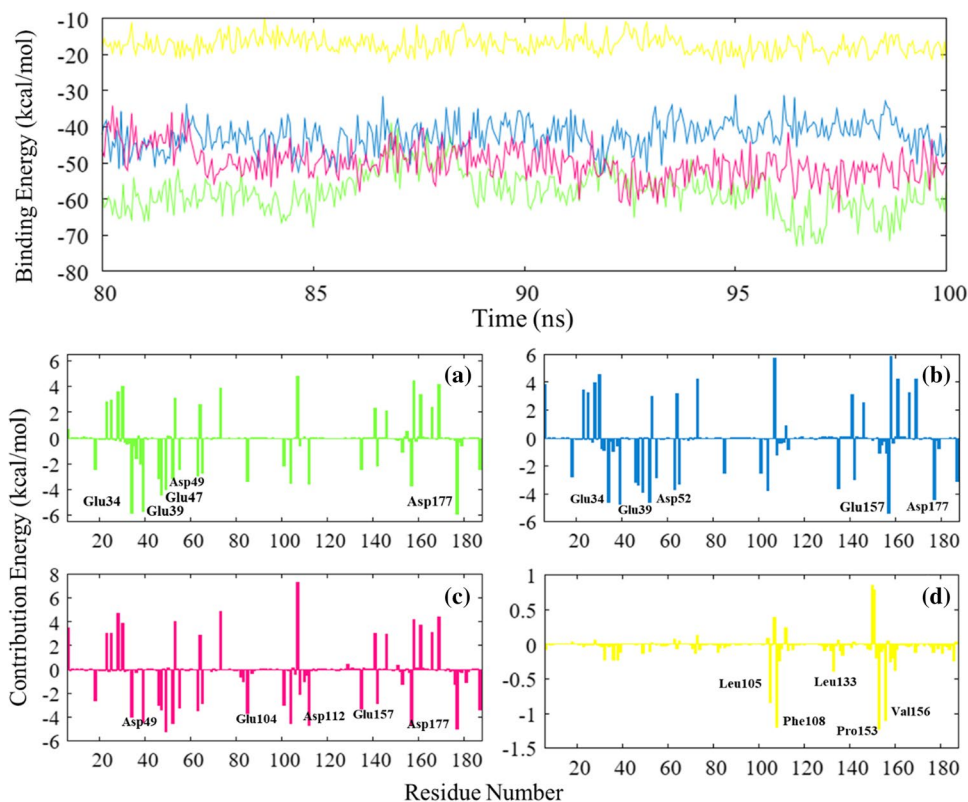
of the AHLS-ZINC000053298428 complex, it was observed that the ligand was oriented in the binding site for the first 20 ns, and then, for the rest of the simulation, it preferred interacting with the surrounding loop region comprising residues Y35-E40. In contrast, MD simulation trajectories of other AHLS systems revealed that ZINC000049037032, ZINC000019796080 and J8-C8 remained positioned at the binding site until the end of their respective MD simulations. Also, the observation was further confirmed by the time-averaged minimum distance calculations between the selected ligands and AHLS. The average minimum distance between AHLS and ZINC000053298428 was 0.24 nm, which was noticeably higher than the average minimum distance values for ZINC000049037032 (0.21 nm), ZINC000019796080 (0.19 nm) and J8-C8 (0.19 nm). Figure 12 depicts the MD simulation snapshots of AHLS complexes captured at 0 ns, 25 ns, 50 ns, 75 ns and 100 ns. The dissociation of ZINC000053298428 from the binding site of AHLS can clearly be observed in the snapshots. Besides, per-residue fluctuations (RMSF) were studied to assess the result of ZINC000053298428 binding to the Y35-E40 loop segment. The average RMSF values of free AHLS, AHLS-ZINC000053298428, AHLS-ZINC000049037032, AHLS-ZINC000019796080 and AHLS-J8-C8 complexes were 0.16 nm, 0.1 nm, 0.14 nm, 0.12 nm and 0.14 nm, respectively. As expected, the data indicated that the binding of ZINC000053298428 restricted the flexibility of the Tyr35-Glu40 loop region and thus had a stabilising effect on it. PCA and modevectors.py script-based analysis were performed to identify the effects of ligand-binding events on the highest magnitude motions experienced by AHLS systems. The plots describing the eigenvalue ranks indicated that, except for the AHLS-ZINC000053298428 complex, the ligand-binding events resulted in increased eigenvector 1 and eigenvector 2 associated conformational changes in AHLS complexes. Moreover, PCA scatter plots of all AHLS systems indicated the presence of considerable conformational shifts in the initial phase of MD simulations. It was followed by the compact clustering of final conformations on the essential subspace, thereby suggesting the convergence of AHLS systems. Modevectors.py script-based analysis of the top two eigenvectors showed that, compared to other AHLS systems, AHLS-ZINC000019796080 and AHLS-J8-C8 complexes experienced the highest magnitude dominant motions, and it also demonstrated that dominant motions in all AHLS systems were mainly localised to the various loop segments. More importantly, the conserved binding site of none of the AHLS systems participated in high magnitude motions.

The FEL analysis suggested that the ligand-binding events induced conformational perturbations in AHLS complexes, especially the AHLS-J8-C8 complex, which exhibited multiple low energy (Gibbs energy content approaching

Table 8 Contribution of energy components involved in complex formation between AHLS and the selected molecules

S/No	System	Van der Waals energy (kcal/mol)	Electrostatic energy (kcal/mol)	Polar solvation energy (kcal/mol)	SASA energy (kcal/mol)	Binding free energy (kcal/mol)
1	AHLS-ZINC000053298428	-29.51 ± 2.35	-62.05 ± 7.86	36.85 ± 7.59	-3.19 ± 0.27	-57.91 ± 5.57
2	AHLS-ZINC000049037032	-36.91 ± 4.22	-77.71 ± 5.74	76.52 ± 5.54	-4.01 ± 0.28	-42.29 ± 4.05
3	AHLS-ZINC000019796080	-43.32 ± 2.99	-88.33 ± 5.93	86.36 ± 8.89	-4.72 ± 0.27	-50.02 ± 4.67
4	AHLS-J8-C8	-29.97 ± 2.71	-13.64 ± 2.33	28.7 ± 3.06	-3.33 ± 0.25	-17.24 ± 2.38

Fig. 11 Binding free energy values and contribution of top five residues of **a** AHLS-ZINC000053298428 (green), **b** AHLS-ZINC000049037032 (blue), **c** AHLS-ZINC000019796080 (Pink), and **d** AHLS-J8-C8 (Yellow)

0 kJ/mol) conformation clusters scattered throughout the FEL plot. On the other hand, the rest of the AHLS-ligand complexes, namely AHLS-ZINC000053298428, AHLS-ZINC000049037032 and AHLS-ZINC000019796080 complexes, exhibited 1 to 2 clusters possessing very low energy (stable) conformations. Also, FEL combined with PCA result suggested that final conformations of the AHLS-ZINC000019796080 complex populated the lowest energy basin in the free energy region. The DCCM analysis indicated that, except for the AHLS-ZINC000053298428 complex, the ligand-binding events increased the global correlated motions in all AHLS complexes. The results also depicted highly correlated motions inside the secondary structure elements of AHLS. Additionally, the analysis showed that ligand-binding events caused a shift of anti-correlated motions from the substrate-binding site to the highly flexible Ser114-A123 loop segment. In case of all

AHLS complexes, the loop segment exhibited substantial anti-correlated motions with respect to proximal secondary structure elements. Finally, the MM/PBSA based binding free energy computations using the last 20 ns of stable trajectories suggested very strong binding interactions between AHLS and the selected ligands. ZINC000053298428, ZINC000049037032 and ZINC000019796080 exhibited binding free energy values of -57.91 ± 5.57 kcal/mol, -42.29 ± 4.05 kcal/mol and -50.02 ± 4.67 kcal/mol, respectively. In comparison, the control molecule achieved the least binding affinity of -17.24 ± 2.38 kcal/mol. The analysis also showed that acidic amino acid residues surrounding the binding site were the top contributors to binding free energy for all the selected AHLS-ligand complexes. Also, the molecules (Z815888654, Z2416029019 and Z3766992625) identified in our previous AHLS study exhibited MM/PBSA binding free energy values between
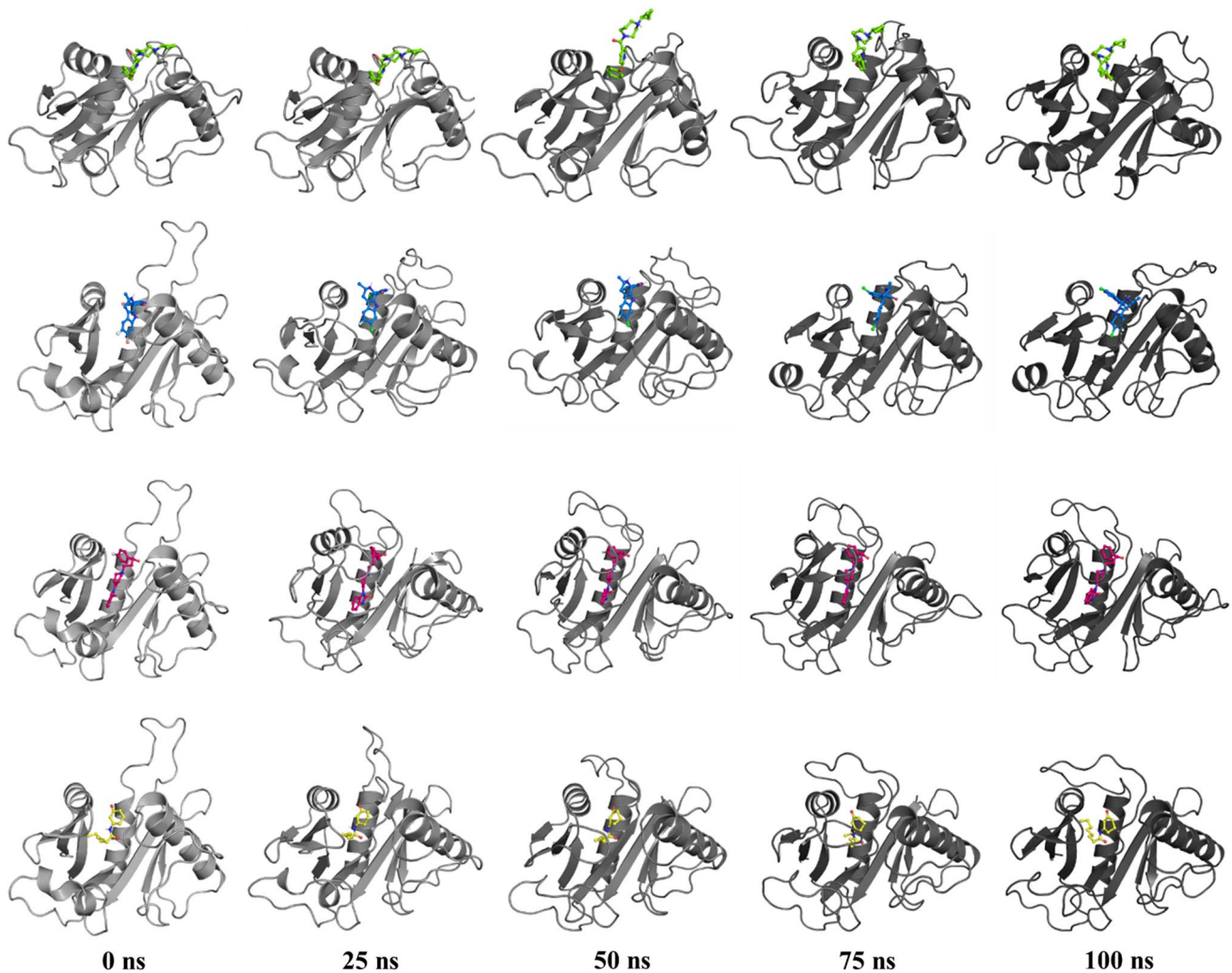
Fig. 12 MD snapshots of AHLS systems captured at successive time points: AHLS- ZINC000053298428 (green), AHLS-ZINC000049037032 (blue), AHLS- ZINC000019796080 (pink), and AHLS-J8-C8 (yellow)

− 21.44 kcal/mol and − 33.68 kcal/mol, which were noticeably higher than the binding free energy values displayed by ZINC000049037032 and ZINC000019796080.

The chosen ligands, namely ZINC000053298428 (DrugBank accession number: DB12929), ZINC000049037032 (DrugBank accession number: DB12306) and ZINC000019796080 (DrugBank accession number: DB00450), have already been studied for their therapeutic properties. ZINC000053298428 or JNJ-39220675 is an investigational drug that belongs to the class of diaryl ether, and it has been previously studied to treat allergic rhinitis [30, 31]. Similarly, ZINC000049037032 or Cipargamin is an investigational drug belonging to the class of harmala alkaloids, and it has been studied for the treatment of malaria [32, 33]. Finally, ZINC000019796080 or Droperidol is an FDA approved drug belonging to the class of alkyl-phenyl ketones, and it is used to treat postoperative nausea and vomiting [34, 35].

Based on the results of virtual screening and docking calculations, toxicity and pharmacokinetic studies, global and essential dynamics and MM/PBSA based free energy calculations, ZINC000019796080 (Droperidol) and ZINC000049037032 (Cipargamin) can be considered as potential inhibitors of the binding site of AHLS from *A. baumannii*. ZINC000019796080 (Droperidol) achieved an excellent MM/PBSA based binding free energy of − 50.02 ± 4.67 kcal/mol towards AHLS, and apart from increased flexibility at the loop segments, the AHLS-ZINC000019796080 complex demonstrated the highest consistency and stability across all MD parameters. Followed by ZINC000019796080, ZINC000049037032 (Cipargamin) also achieved a very high MM/PBSA based binding free energy of − 42.29 ± 4.05 kcal/mol towards

AHLS, its binding didn't much increase the flexibility of loop segments, and the AHLS-ZINC000049037032 complex also demonstrated a high degree of stability across all MD parameters. Furthermore, contrary to the virtual screening and docking results, the MD simulation results suggested that ZINC000053298428 (JNJ-39220675) failed as a lead candidate because it disassociated from the binding site at approximately 20 ns time point and preferred binding to a surrounding loop segment for the rest of simulation period.

Conclusion

Multi-drug resistant strains of *A. baumannii* have periodically been identified as causative agents of healthcare-associated infections, including hospital-acquired pneumonia, meningitis and urinary tract infection [36, 37]. Owing to the advent of multi-drug resistant strains of *A. baumannii*, it is crucial to identify novel molecules capable of inhibiting enzymes involved in its major biosynthetic pathways. Therefore, the present study has employed extensive computational investigation to identify potential inhibitors of the substrate-binding site of AHLS, an enzyme involved in the quorum-sensing pathway. As a result, three molecules (JNJ-39220675, Cipargamin and Droperidol) were identified based on the results obtained from Vina, Lipinski's and toxicity screening, and ADME screening. Finally, based on the results of global and essential dynamics analyses, two of these molecules (Droperidol and Cipargamin) were identified as strong binders of the binding site of AHLS. Droperidol, an FDA-approved postoperative nausea drug, and Cipargamin, an investigational malaria drug, achieved binding free energy values of -50.02 ± 4.67 kcal/mol and -42.29 ± 4.05 kcal/mol, respectively. Therefore, if experimentally verified, the identified molecules can aid in drug development efforts against multi-drug resistant strains of *A. baumannii*.

Declarations

Conflict of interest None.

References

1. Howard A, O'Donoghue M, Feeney A, Sleator RD (2012) *Acinetobacter baumannii*: an emerging opportunistic pathogen. Virulence 3:243–250. https://doi.org/10.4161/viru.19700

2. Al-Anazi KA, Abdalhamid B, Alshibani Z, Awad K, Alzayed A, Hassan H, Alsayiegh M (2012) *Acinetobacter baumannii* septicemia in a recipient of an allogeneic hematopoietic stem cell transplantation. Case Rep Transpl 2012:646195. https://doi.org/10.1155/2012/646195

3. Ni S, Li S, Yang N, Zhang S, Hu D, Li Q, Lu M (2015) Post-neurosurgical meningitis caused by *Acinetobacter baumannii*: case series and review of the literature. Int J Clin Exp Med 8:21833–21838

4. Chaari A, Mnif B, Bahloul M, Mahjoubi F, Chtara K, Turki O, Gharbi N, Chelly H, Hammami A, Bouaziz M (2013) *Acinetobacter baumannii* ventilator-associated pneumonia: epidemiology, clinical characteristics, and prognosis factors. Int J Infect Dis 17:e1225-1228. https://doi.org/10.1016/j.ijid.2013.07.014

5. Hartzell JD, Kim AS, Kortepeter MG, Moran KA (2007) Acinetobacter pneumonia: a review. MedGenMed 9:4

6. Rao RS, Karthika RU, Singh SP, Shashikala P, Kanungo R, Jayachandran S, Prashanth K (2008) Correlation between biofilm production and multiple drug resistance in imipenem resistant clinical isolates of *Acinetobacter baumannii*. Indian J Med Microbiol 26:333–337. https://doi.org/10.4103/0255-0857.43566

7. Daniels R, Vanderleyden J, Michiels J (2004) Quorum sensing and swarming migration in bacteria. FEMS Microbiol Rev 28:261–289. https://doi.org/10.1016/j.femsre.2003.09.004

8. Atkinson S, Chang CY, Sockett RE, Camara M, Williams P (2006) Quorum sensing in Yersinia enterocolitica controls swimming and swarming motility. J Bacteriol 188:1451–1461. https://doi.org/10.1128/JB.188.4.1451-1461.2006

9. Lade H, Paul D, Kweon JH (2014) N-acyl homoserine lactone-mediated quorum sensing with special reference to use of quorum quenching bacteria in membrane biofouling control. Biomed Res Int 2014:162584. https://doi.org/10.1155/2014/162584

10. Saipriya K, Swathi CH, Ratnakar KS, Sritharan V (2020) Quorum-sensing system in *Acinetobacter baumannii*: a potential target for new drug development. J Appl Microbiol 128:15–27. https://doi.org/10.1111/jam.14330

11. Bindu Subhadra MHO, Choi CH (2016) Quorum sensing in Acinetobacter: with special emphasis on antibiotic resistance, biofilm formation and quorum quenching. AIMS Microbiol 2:27–41. https://doi.org/10.3934/microbiol.2016.1.27

12. Jha RK, Jabeer Khan R, Singh E, Kumar A, Jain M, Muthukumaran J, Singh AK (2022) An extensive computational study to identify potential inhibitors of Acyl-homoserine-lactone synthase from *Acinetobacter baumannii* (strain AYE). J Mol Graph Model 114:108168. https://doi.org/10.1016/j.jmgm.2022.108168

13. Waterhouse A, Bertoni M, Bienert S, Studer G, Tauriello G, Gumienny R, Heer FT, de Beer TAP, Rempfer C, Bordoli L et al (2018) SWISS-MODEL: homology modelling of protein structures and complexes. Nucleic Acids Res 46:W296–W303. https://doi.org/10.1093/nar/gky427

14. Krieger E, Joo K, Lee J, Lee J, Raman S, Thompson J, Tyka M, Baker D, Karplus K (2009) Improving physical realism, stereochemistry, and side-chain accuracy in homology modeling: four

approaches that performed well in CASP8. Proteins 77(Suppl 9):114–122. https://doi.org/10.1002/prot.22570

15. Trott O, Olson AJ (2010) AutoDock Vina: improving the speed and accuracy of docking with a new scoring function, efficient optimization, and multithreading. J Comput Chem 31:455–461. https://doi.org/10.1002/jcc.21334

16. Sander T, Freyss J, von Korff M, Rufener C (2015) DataWarrior: an open-source program for chemistry aware data visualization and analysis. J Chem Inf Model 55:460–473. https://doi.org/10.1021/ci500588j

17. Daina A, Michielin O, Zoete V (2017) SwissADME: a free web tool to evaluate pharmacokinetics, drug-likeness and medicinal chemistry friendliness of small molecules. Sci Rep 7:42717. https://doi.org/10.1038/srep42717

18. Chung J, Goo E, Yu S, Choi O, Lee J, Kim J, Kim H, Igarashi J, Suga H, Moon JS et al (2011) Small-molecule inhibitor binding to an N-acyl-homoserine lactone synthase. Proc Natl Acad Sci U S A 108:12089–12094. https://doi.org/10.1073/pnas.1103165108

19. Morris GM, Huey R, Lindstrom W, Sanner MF, Belew RK, Goodsell DS, Olson AJ (2009) AutoDock4 and AutoDockTools4: automated docking with selective receptor flexibility. J Comput Chem 30:2785–2791. https://doi.org/10.1002/jcc.21256

20. BIOVIA DS (2019) Discovery studio visualization Dassault Systèmes BIOVIA

21. Van Der Spoel D, Lindahl E, Hess B, Groenhof G, Mark AE, Berendsen HJC (2005) GROMACS: fast, flexible, and free. 26:1701–1718. https://doi.org/10.1002/jcc.20291

22. Huang W, Lin Z, van Gunsteren WF (2011) Validation of the GROMOS 54A7 force field with respect to beta-peptide folding. J Chem Theory Comput 7:1237–1243. https://doi.org/10.1021/ct100747y

23. Schuttelkopf AW, van Aalten DM (2004) PRODRG: a tool for high-throughput crystallography of protein-ligand complexes. Acta Crystallogr D 60:1355–1363. https://doi.org/10.1107/S0907444904011679

24. Grant BJ, Rodrigues AP, ElSawy KM, McCammon JA, Caves LS (2006) Bio3d: an R package for the comparative analysis of protein structures. Bioinformatics 22:2695–2696. https://doi.org/10.1093/bioinformatics/btl461

25. Genheden S, Ryde U (2015) The MM/PBSA and MM/GBSA methods to estimate ligand-binding affinities. Expert Opin Drug Discov 10:449–461. https://doi.org/10.1517/17460441.2015.1032936

26. Kumari R, Kumar R, Lynn A (2014) g_mmpbsa–a GROMACS tool for high-throughput MM-PBSA calculations. J Chem Inf Model 54:1951–1962. https://doi.org/10.1021/ci500020m

27. Chen J, Sawyer N, Regan L (2013) Protein-protein interactions: general trends in the relationship between binding affinity and interfacial buried surface area. Protein Sci 22:510–515. https://doi.org/10.1002/pro.2230

28. Kabsch W, Sander C (1983) Dictionary of protein secondary structure: pattern recognition of hydrogen-bonded and geometrical features. Biopolymers 22:2577–2637. https://doi.org/10.1002/bip.360221211

29. Chakravarty D, Guharoy M, Robert CH, Chakrabarti P, Janin J (2013) Reassessing buried surface areas in protein-protein complexes. Protein Sci 22:1453–1457. https://doi.org/10.1002/pro.2330

30. Barchuk WT, Salapatek AM, Ge T, D'Angelo P, Liu X (2013) A proof-of-concept study of the effect of a novel H3-receptor antagonist in allergen-induced nasal congestion. J Allergy Clin Immunol 132(838–846):e831-836. https://doi.org/10.1016/j.jaci.2013.05.001

31. Logan J, Carruthers NI, Letavic MA, Sands S, Jiang X, Shea C, Muench L, Xu Y, Carter P, King P et al (2012) Blockade of the brain histamine H3 receptor by JNJ-39220675: preclinical PET studies with [11C]GSK189254 in anesthetized baboon. Psychopharmacology 223:447–455. https://doi.org/10.1007/s00213-012-2733-x

32. Hien TT, White NJ, Thuy-Nhien NT, Hoa NT, Thuan PD, Tarning J, Nosten F, Magnusson B, Jain JP, Hamed K (2017) Estimation of the in vivo MIC of cipargamin in uncomplicated plasmodium falciparum malaria. Antimicrob Agents Chemother. https://doi.org/10.1128/AAC.01940-16

33. Bouwman SA, Zoleko-Manego R, Renner KC, Schmitt EK, Mombo-Ngoma G, Grobusch MP (2020) The early preclinical and clinical development of cipargamin (KAE609), a novel antimalarial compound. Travel Med Infect Dis 36:101765. https://doi.org/10.1016/j.tmaid.2020.101765

34. Hirata I, Iwamoto M, Matsui H, Yoshinuma H, Funakoshi R (2020) Droperidol reduces postoperative nausea and vomiting and supports the continuation of intravenous patient-controlled analgesia with fentanyl. J Pharm Pharm Sci 23:220–230. https://doi.org/10.18433/jpps30902

35. Schaub I, Lysakowski C, Elia N, Tramer MR (2012) Low-dose droperidol (</=1 mg or </=15 mug kg-1) for the prevention of postoperative nausea and vomiting in adults: quantitative systematic review of randomised controlled trials. Eur J Anaesthesiol 29:286–294. https://doi.org/10.1097/EJA.0b013e328352813f

36. Dijkshoorn L, Nemec A, Seifert H (2007) An increasing threat in hospitals: multidrug-resistant *Acinetobacter baumannii*. Nat Rev Microbiol 5:939–951. https://doi.org/10.1038/nrmicro1789

37. Cornejo-Juarez P, Cevallos MA, Castro-Jaimes S, Castillo-Ramirez S, Velazquez-Acosta C, Martinez-Oliva D, Perez-Oseguera A, Rivera-Buendia F, Volkow-Fernandez P (2020) High mortality in an outbreak of multidrug resistant *Acinetobacter baumannii* infection introduced to an oncological hospital by a patient transferred from a general hospital. PLoS ONE 15:e0234684. https://doi.org/10.1371/journal.pone.0234684